

C–O–H–S fluids and granitic magma: how S partitions and modifies CO₂ concentrations of fluid-saturated felsic melt at 200 MPa

J. D. Webster · B. Goldoff · N. Shimizu

Received: 10 November 2010 / Accepted: 21 March 2011 / Published online: 3 April 2011
© Springer-Verlag 2011

Abstract Hydrothermal volatile-solubility and partitioning experiments were conducted with fluid-saturated haplogranitic melt, H₂O, CO₂, and S in an internally heated pressure vessel at 900°C and 200 MPa; three additional experiments were conducted with iron-bearing melt. The run-product glasses were analyzed by electron microprobe, FTIR, and SIMS; and they contain ≤ 0.12 wt% S, ≤ 0.097 wt% CO₂, and ≤ 6.4 wt% H₂O. Apparent values of $\log f_{O_2}$ for the experiments at run conditions were computed from the $[(S^{6+})/(S^{6+}+S^{2-})]$ ratio of the glasses, and they range from NNO -0.4 to NNO $+1.4$. The C–O–H–S fluid compositions at run conditions were computed by mass balance, and they contained 22–99 mol% H₂O, 0–78 mol% CO₂, 0–12 mol% S, and <3 wt% alkalis. Eight S-free experiments were conducted to determine the H₂O and CO₂ concentrations of melt and fluid compositions and to compare them with prior experimental results for C–O–H fluid-saturated rhyolite melt, and the agreement is excellent. Sulfur partitions very strongly in favor of fluid in all experiments, and the presence of S modifies the fluid compositions, and hence, the CO₂ solubilities in coexisting felsic melt. The square of the mole fraction of H₂O in melt increases in a linear fashion, from 0.05 to 0.25, with the

H₂O concentration of the fluid. The mole fraction of CO₂ in melt increases linearly, from 0.0003 to 0.0045, with the CO₂ concentration of C–O–H–S fluids. Interestingly, the CO₂ concentration in melts, involving relatively reduced runs ($\log f_{O_2} \leq \text{NNO} + 0.3$) that contain 2.5–7 mol% S in the fluid, decreases significantly with increasing S in the system. This response to the changing fluid composition causes the H₂O and CO₂ solubility curve for C–O–H–S fluid-saturated haplogranitic melts at 200 MPa to shift to values near that modeled for C–O–H fluid-saturated, S-free rhyolite melt at 150 MPa. The concentration of S in haplogranitic melt increases in a linear fashion with increasing S in C–O–H–S fluids, but these data show significant dispersion that likely reflects the strong influence of f_{O_2} on S speciation in melt and fluid. Importantly, the partitioning of S between fluid and melt does not vary with the (H₂O/H₂O + CO₂) ratio of the fluid. The fluid-melt partition coefficients for H₂O, CO₂, and S and the atomic (C/S) ratios of the run-product fluids are virtually identical to thermodynamic constraints on volatile partitioning and the H, S, and C contents of pre-eruptive magmatic fluids and volcanic gases for subduction-related magmatic systems thus confirming our experiments are relevant to natural eruptive systems.

Communicated by T. L. Grove.

J. D. Webster (✉) · B. Goldoff
Department of Earth and Planetary Sciences, American Museum of Natural History, Central Park West at 79th Street,
New York, NY 10024-5192, USA
e-mail: jdw@amnh.org

N. Shimizu
Geology and Geophysics Department, Woods Hole
Oceanographic Institution, 360 Woods Hole Road, MS 23,
Woods Hole, MA 02543-1541, USA

Keywords Volatile solubility · H₂O · CO₂ · S · Degassing · Granite melt · Multi-component fluid

Introduction

Explosive volcanism typically involves fluid-saturated, intermediate-silica-content to felsic magmas largely enriched in H₂O and containing lesser but variable concentrations of CO₂, S, halogens, and other volatile and fluxing

constituents. Interpretation of processes of magmatic fluid exsolution, fluid evolution, and subsequent surficial degassing through geochemical research calls for experimental and thermodynamic constraints on the solubilities of H₂O, CO₂, and S in a variety of silicate melts over a range of mantle and crustal pressures and temperatures. At present, systematic experimental studies of solubilities and partitioning behavior of volatile components in fluid-saturated felsic melts are limited to individual and binary volatile pseudosystems involving melt plus H₂O ± CO₂ (Holloway and Blank 1994; Tamic et al. 2001; Moore 2008), H₂O ± S (Scaillet et al. 1998; Keppler 1999, 2010); Clemente et al. 2004; Burgisser et al. 2008, or H₂O-Cl (Webster 1992a, b). Some recent studies, however, offer promise because they involve experimental investigation of O–H ± C ± S ± Cl ± F-bearing fluids and a variety of aluminosilicate melts (Botcharnikov et al. 2004; Spilliaert et al. 2006; Nicholis and Rutherford 2009; Botcharnikov et al. 2005; Webster et al. 2006, 2009; Parat et al. 2008; Teague et al. 2008; Beermann 2010), but most of them have involved basaltic to intermediate-silica melts. Currently, we lack a detailed experimental analysis of volatile solubility behavior in C–O–H–S fluids coexisting with felsic melts at shallow crustal pressure. This report describes the results of experimentally constrained concentrations of H₂O, CO₂, and S in C–O–H–S fluids and haplogranitic melt at 200 MPa, temperatures of 895–912°C, and apparent log *f*_{O₂} ranging from NNO –0.4 to NNO + 1.4. This research has also determined the partitioning behavior of H₂O, CO₂, and S between the melt and fluids as a function of bulk fluid composition and *f*_{O₂}.

Methods

Experimental

A haplogranitic glass—chemically equivalent to the haplogranite minimum-melt composition at P_{H₂O} = 200 MPa, having a molar (Al₂O₃/Na₂O + K₂O) of 1.0 and a molar (Na₂O/Na₂O + K₂O) of 0.59, and synthesized by Corning Incorporated—was provided for this study by David London (Table 1). The glass was crushed to a fine powder and used for the silicate starting material. Carbon was added to the starting charges as C₂H₂O₄·2H₂O, PdC₂O₄, or Ag₂C₂O₄. Sulfur was added as elemental sulfur, as an aqueous solution of Na₂SO₄ and K₂SO₄ containing 2.5 wt% S and characterized by a molar (Na₂O/Na₂O + K₂O) of 0.6, or as both. For most S-bearing experiments, the CO₂ was added as oxalic acid dihydrate to avoid reaction of S with Pd or Ag, but for one S-bearing run (e.g., 1-08-05A), CO₂ was added as silver oxalate. Water was added as distilled and de-ionized H₂O with or without oxalic acid dihydrate and

the aqueous Na₂SO₄ and K₂SO₄ solution. Three S-bearing experiments involved iron added as reagent-grade Fe₃O₄. The twenty-two experiments that included S were conducted in gold capsules, and the eight other S-free runs were conducted in platinum. The calculated (fluid/melt) mass ratios at run conditions ranged from 0.03 to 0.46.

The experiments were conducted in an internally heated pressure vessel (IHPV) at the American Museum of Natural History (AMNH). Pressure was monitored with Heise gauges, and temperature with two chromel–alumel thermocouples the tips of which span the length of the experimental capsules. All experiments were quenched isobarically. The IHPV provides a relatively rapid quench; run temperature decreased from 900° to <500°C in 10 s or less.

For most experiments, temperature ranged from 895 to 912°C and pressure from 199 to 204 MPa, but one S-free run was conducted at 1,100°C. The experiments ranged from 142 to 725 h in duration. During the runs, most capsules were simply exposed to the intrinsic *f*_{H₂} of the steel walls of the IHPV. The log *f*_{O₂} imposed by this *f*_{H₂} is equivalent to NNO + 2 log units at 200 MP, 800°C, and with activity of H₂O, *a*_{H₂O}, of unity (as determined with an oxygen sensor), but the final *f*_{O₂} of most runs was likely lower because the *X*_{H₂O}^{fl} were less than unity and, hence, the *X*_{H₂O} was less than unity (described below). For three experiments involving a total of six individual capsules, the capsules were run at more reducing conditions by exposing them to H₂ added to the Ar pressure medium via a Shaw membrane. As detailed in the following results description, the apparent log *f*_{O₂} of most S-bearing runs was calculated from the measured [(S⁶⁺)/(S⁶⁺ + S²⁻)] ratio of the glasses, and it ranges from NNO –0.4 to NNO + 1.4 although most are between NNO and NNO + 0.9. We have no constraints on the *f*_{S₂} of these experiments.

Regarding the approach to equilibrium, it should be noted that these runs began with S in the starting fluid (±elemental S) and the starting glass contained no S. Equilibrium requires sufficient diffusion of S into the melt (provided by the fluid) to generate a homogeneous melt composition and acquisition of an equilibrium distribution of S in the melt as S^{–2} and S⁺⁶ for the *f*_{O₂} relevant to each run. Our ca. 900°C-run durations ranged from ca. 6–18 days for most experiments, but one run was conducted for 30 days. In comparison, most of the S-partitioning experiments of Keppler (2010) involving O–H–S fluid-saturated haplogranite melts were conducted for 20–40 days but at lower temperatures (750–850°C at 50–300 MPa). As shown below, our S-partitioning data generally agree with those of Keppler (2010). Moreover, four of our experiments (e.g., runs 1-08-05C, 1-08-06C, 1-08-14A, and 1-10-02B; Table 2) show remarkable consistency in their S partitioning between fluid and melt and

Table 1 Experimental run conditions and run-product glass compositions (by wet chemistry and electron microprobe in wt%)

Glass (run) ID	P (MPa)	T (°C)	Duration (h)	f_{H_2} (bars)	SiO ₂	Al ₂ O ₃	Na ₂ O	K ₂ O	FeO	S	Total	H ₂ O	CO ₂	N/NK	A/NK	S by SIMS
Wt. chem.					77.68	12.70	4.49	4.85	0.00	0.00	99.70			0.59	1.0	
EPMA-FTIR					78.15	12.79	4.50	4.79	0.00	0.00	100.23	0.03	n.d.	0.59	1.01	
1-08-02B	203	900	406	amb.	73.08	12.21	4.19	4.44	0.00	0.00	93.91	5.69	0	0.59	1.04	
1-08-03A	199	900	215	amb.	72.16	12.19	4.45	5.09	0.00	0.045	93.93	5.84	0	0.57	0.95	0.044
1-08-03B	199	900	215	amb.	72.55	12.30	4.32	4.65	0.00	0.055	93.87	5.87	0	0.59	1.01	
1-08-03C	199	900	215	amb.	73.28	12.24	4.51	4.97	0.00	0.035	95.03	4.75	0.004	0.58	0.96	0.038
1-08-04A	199	900	333	amb.	73.00	12.97	4.77	4.77	0.00	0.005	95.52	4.83	0.008	0.60	1.00	
1-08-04B	199	900	333	amb.	73.00	12.92	4.71	4.79	0.00	0.005	95.43	4.72	0.006	0.60	1.00	0.002
1-08-04C	199	900	333	amb.	74.21	12.58	4.50	4.64	0.00	0.025	95.95	6.16	0	0.60	1.01	0.031
1-08-05A ^a	200	900	142	amb.	75.46	12.60	4.53	4.62	0.00	0.003	97.21	3.32	0.034	0.60	1.01	0.015
1-08-05B	200	900	142	amb.	73.08	12.51	4.32	4.81	0.00	0.075	94.78	5.84	0	0.58	1.02	
1-08-05C	200	900	142	amb.	72.48	12.28	4.17	4.56	0.00	0.055	93.55	6.39	0	0.58	1.04	0.06
1-08-06A	204	909	292	amb.	74.98	12.46	4.46	4.58	0.00	0.00	96.48	3.08	0.084	0.60	1.01	
1-08-06B	204	909	292	amb.	75.27	12.67	4.43	4.57	0.00	0.015	96.95	2.68	0.073	0.60	1.04	
1-08-06C	204	909	292	amb.	73.88	12.45	4.53	4.67	0.00	0.04	95.57	4.01	0.057	0.60	1.00	0.031
1-08-07A	201	897	290	amb.	73.26	12.11	4.34	4.75	0.00	0.03	94.49	5.25	0.02	0.58	0.99	0.029
1-08-07B	201	897	290	amb.	72.45	12.19	4.33	4.64	0.00	0.03	93.64	5.48	0.011	0.59	1.00	0.032
1-08-07C	201	897	290	amb.	72.55	12.06	4.31	4.73	0.00	0.03	93.68	5.4	0.009	0.58	0.99	
1-08-11A	200	1,100	215	amb.	73.98	12.27	4.13	4.59	0.00	0.00	94.97	5.21	0.009	0.58	1.04	
1-08-12	199	905	431	2.8	74.25	12.25	4.54	4.92	0.00	0.02	95.98	4.52	0.009	0.58	0.96	
1-08-14A	204	895	725	amb.	73.09	12.07	4.44	4.92	0.00	0.04	94.56	4.93	0.027	0.58	0.96	
1-08-14B	204	895	725	amb.	73.96	12.13	4.18	4.83	0.00	0.11	95.21	4.92	0.026	0.57	1.00	
1-09-10A	204	907	141	amb.	71.70	12.33	4.05	4.30	0.00	0.00	92.38	5.94	0	0.59	1.09	0.0007
1-09-10B	204	907	141	amb.	74.09	12.26	4.22	4.43	0.00	0.00	95.01	4.32	0.053	0.59	1.04	0.0006
1-09-10C	204	907	141	amb.	76.11	12.56	4.34	4.35	0.00	0.00	97.36	2.56	0.097	0.60	1.06	0.0007
1-10-01A	200	912	213	amb.	75.80	12.92	4.57	4.74	0.00	0.00	98.03	2.27	0.097	0.59	1.02	0.0008
1-10-01B	200	912	213	amb.	75.70	12.84	4.50	4.76	0.00	0.00	97.8	2.45	0.094	0.59	1.02	0.0017
1-10-02A	200	899	186	22.6	74.07	12.95	4.81	4.90	0.00	0.005	96.74	3.93	0.029	0.60	0.98	
1-10-02B	200	899	186	22.6	74.72	12.95	4.61	4.87	0.00	0.01	97.17	5.35	0.016	0.59	1.01	
1-10-15A	200	899	213	20.6	73.39	12.12	3.87	4.77	1.04	0.11	95.31	4.25	0.033	0.55	1.05	
1-10-15B	200	899	213	20.6	73.16	12.31	4.07	4.48	1.16	0.096	95.27	3.98	0.043	0.58	1.07	
1-10-15C	200	899	213	20.6	72.98	12.38	4.10	4.48	1.08	0.095	95.12	3.37	0.044	0.58	1.07	

Bold font sulfur-free runs. All runs conducted in gold capsules except 1-08-02B, 1-08-11A&B, 1-09-10A & B & C, 1-10-01A & B which were conducted in Pt

Start Wt. chem. starting haplogranite glass composition determined by wet chemical analysis; *start EPMA-FTIR* shows results of analyses of same glass with AMNH electron microprobe and FTIR (see text for details on “[Methods](#)”). Runs 1-10-15 A/B/C conducted with Fe added as magnetite

n.d. constituent not detected

amb. experiment subjected to the ambient or intrinsic hydrogen fugacity of the pressure vessel which provides an the effective log f_{O_2} equivalent to NNO + 2 log units for water-saturated conditions at 200 MPa and 800°C

H₂O and CO₂ determined by FTIR (see text for details on “[Methods](#)”)

N/NK molar (Na₂O/Na₂O + K₂O)

A/NK molar (Al₂O₃/Na₂O + K₂O)

^a Sole run conducted with CO₂ added as Ag₂C₂O₄ and some S may have been consumed by reaction with Ag, resulting in low f_{S_2}

in their apparent values of f_{O_2} even though they were conducted for durations ranging from ca. 6 to 30 days. This consistency in the extent of S partitioning over 6–30 days

and the general agreement with the data of Keppler (2010) suggest a reasonable approach to equilibrium at these conditions.

Although our experiments were conducted well below the melting point of pure gold, the use of multiple gold capsules, simultaneously, typically led to sintering and adhesion of the capsules to one another, and this made it difficult to separate the capsules without causing leakage

after the run. Consequently, we observed microscopic droplets of run-product liquid on the exterior of several of the capsules after the runs were quenched. The presence of liquid droplets indicates that the leakage occurred during and/or after the quench; the fluid should have boiled away

Table 2 Experimental run conditions, composition of fluids at run conditions, and partition coefficients ([fluid/melt] in mol% and wt%) for volatiles at 900°C and 200 MPa

Glass (run) ID	f_{H_2} (bars)	App Δf_{O_2}	Mol% $\text{H}_2\text{O}^{\text{fl}}$	Mol% CO_2^{fl}	Mol% $S_{\text{total}}^{\text{fl}}$	WT $D_{\text{H}_2\text{O}}^{\text{fl/mt}}$	WT $D_{\text{CO}_2}^{\text{fl/mt}}$	WT $D_{\text{S}}^{\text{fl/mt}}$	Molar $D_{\text{H}_2\text{O}}^{\text{fl/mt}}$	Molar $D_{\text{CO}_2}^{\text{fl/mt}}$	Molar $D_{\text{S}}^{\text{fl/mt}}$	Molar (C/S) ^{fl}	$[(\text{S}^{6+})/(\text{S}^{6+}+\text{S}^{2-})]$
1-08-02B	amb.		99	0	0	18			316				
1-08-03A	amb.	+0.89	88.4	0	7.2	14		278	273		5,440		0.73
1-08-03B	amb.	+0.37	91.5	0	6.2	15		185	281		3,556		0.45
1-08-03C	amb.	+0.15	73.2	17.1	6.8	12	7,903	266	277	188,010	6,323	2.5	0.32
1-08-04A	amb.		77.8	20.0	0.6	12	4,683	149	290	110,067	2,913	33.3	
1-08-04B	amb.		73.6	24.0	0.7	11	6,630	153	281	162,920	3,766	34.3	
1-08-04C	amb.	+0.69	93.4	0	4.8	14		359	273		6,799		0.63
1-08-05A ^a	amb.		[47.6] ^b	[42.3] ^b	[3.1] ^b								
1-08-05B	amb.	+0.33	87.7	0	10.5	14		226	270		4,464		0.43
1-08-05C	amb.	+0.51	90.7	0	6.3	13		195	255		3,763		0.53
1-08-06A	amb.		43.8	56.2	0	8	902		256	29,410			
1-08-06B	amb.	+0.11	43.3	54.1	2.6	9	1,005	169	291	32,624	5,460	21.2	0.31
1-08-06C	amb.	+0.51	57.9	36.4	4.3	9	995	121	260	28,102	3,436	8.5	0.53
1-08-07A	amb.	+1.45	79.7	17.7	1.4	12	1,698	67	273	38,978	1,544	12.6	0.91
1-08-07B	amb.	+0.48	88.1	10.0	1.0	14	1,918	50	290	39,986	1,041	10	0.51
1-08-07C	amb.	+0.38	87.0	10.3	1.1	14	2,387	59	290	50,226	1,247	9.4	0.46
1-08-11A	amb.		99.9	0.1	0	16	2,020		317	40,756			
1-08-12	2.8	+0.26	69.4	25.1	4.2	11	4,642	271	276	117,430	6,842	6	0.38
1-08-14A	amb.	+0.51	76.3	16.8	5	12	1,176	161	279	27,417	3,763	3.4	0.53
1-08-14B	amb.	+0.63	77.4	8.8	11.6	13	665	156	283	14,776	3,256	0.8	0.60
1-09-10A	amb.		99	0	0	17							
1-09-10B	amb.		71.8	28.2	0	12	919		299	23,283			
1-09-10C	amb.		26.0	74.0	0	5	906		183	33,759			
1-10-01A	amb.		22.3	77.7	0	5	920		177	35,151			
1-10-01B	amb.		23.7	76.3	0	5	940		174	35,574			
1-10-02A	22.6	-0.39	56.8	38.5	3.2	9	2,000	311	260	57,320	8,920	12	0.12
1-10-02B	22.6	+0.53	84.7	12.8	1.8	14	1,747	162	294	37,837	3,519	7.1	0.54
1-10-15A ^b	20.6	+0.22	[73.6] ^b	[14.9] ^b	[9.4] ^b								0.36
1-10-15B ^b	20.6	+0.29	[76.5] ^b	[15.7] ^b	[5.7] ^b								0.40
1-10-15C ^b	20.6	+0.12	[74.6] ^b	[15.6] ^b	[7.8] ^b								0.31

Bold font sulfur-free runs

amb. experiment subjected to the ambient or intrinsic f_{H_2} of the pressure vessel which provides an the effective log f_{O_2} equivalent to NNO + 2 log units for water-saturated conditions at 200 MPa and 800°C

$[(\text{S}^{6+})/(\text{S}^{6+}+\text{S}^{2-})]$ = the mole fraction of oxidized, hexavalent S in the glasses

App Δf_{O_2} apparent value of the log of the oxygen fugacity relative to the NNO solid oxide buffer, computed from $[(\text{S}^{6+})/(\text{S}^{6+}+\text{S}^{2-})]_{\text{glass}}$; see “Methods” in text

The fluids also contained ≤ 3 wt% alkali component which is included in the computations but not reported here (i.e., the fluid totals = $\text{H}_2\text{O} + \text{CO}_2 + \text{S} + \text{alkalis}$)

^a Sole run conducted with CO_2 added as $\text{Ag}_2\text{C}_2\text{O}_4$ and much of the S may have been consumed by reaction with Ag, resulting in reduced f_{S_2}

^b Starting fluid compositions [X mol%] reported for run 1-08-05A and run 1-10-15A/B/C (at pressure and temperature before H_2O , CO_2 , and S in fluid are dissolved by melt) because some S may have been sequestered from melt and fluid by silver sulfide and iron sulfide formation, respectively

if the leakage occurred at $T > 100^\circ\text{C}$. For these runs the glass compositions were analyzed and the fluid compositions calculated by mass balance, even though we could not apply the freeze-and-puncture gravimetric procedure described below.

Analytical

Electron microprobe (EPMA)

The run-product glasses were analyzed for SiO_2 , Al_2O_3 , Na_2O , K_2O , and $\text{S} \pm \text{FeO}$ at 15 keV with a Cameca SX-100 electron microprobe at the AMNH (Table 1). In the first analytical pass, Na_2O , K_2O , and $\text{SiO}_2 \pm \text{FeO}$ were analyzed with a beam current of 2 nA, and Al_2O_3 and S were analyzed at 10 nA in the second pass. The standards for S analysis include troilite and barite depending on the S oxidation state (determined with the method outlined below). Troilite was used for glasses with $[(\text{S}^{6+})/(\text{S}^{6+} + \text{S}^{2-})] < 0.4$, and barite for all other, more oxidized glasses. Peak count times varied from 30 to 60 s. All glasses were analyzed with a defocused, 5–10 μm diameter electron beam, and the glasses were moved during analyses in order to minimize Na and K migration. The reported glass compositions represent the average of four to eight analyses of different spots in the same sample. A variety of internal “standard” glasses (e.g., the anhydrous haplogranitic starting glass; Macusani rhyolitic obsidian; and the NBS 610, 620, and 621 reference materials) were analyzed regularly to check for accuracy and precision (i.e., for instrumental drift) during the course of this experimental investigation. Repeated analyses of the NBS 620 glass, known to contain 0.112 ± 0.01 wt% S, returned a mean S concentration of 0.13 ± 0.006 wt% (1σ).

The oxidation state of S, i.e., oxidized (S^{6+}) and reduced (S^{2-}), was determined by measuring the wavelengths of the S K_α X-rays. This method works because S^{6+} emits shorter wavelengths than S^{2-} and because shifts in the wavelength (λ) of S K_α X-rays relate directly to changes in oxidation state (Carroll and Rutherford 1988; Matthews et al. 1999). One can deduce the S oxidation state of an unknown glass through comparison of S peak positions for unknowns with reference materials such as BaSO_4 and FeS . We analyzed the S K_α radiation in the run-product glasses with EPMA wavelength-dispersive spectrometry and an LPET crystal. We counted the X-rays with a spectrometer $\sin \theta$ range of 0.61158–0.61658 using $\sin \theta$ steps of 0.00002 and a dwell time of 100 ms/step. We rastered a 6- μm beam diameter over a $30 \times 30 \mu\text{m}$ area to avoid oxidation effects resulting from localized heating due to prolonged beam exposure (Wallace and Carmichael 1994; Métrich and Clochiatti 1996). The electron beam was set at 15 keV and 40 nA current. We used 8 accumulations on the reference

standards BaSO_4 and FeS , and 30-scan accumulations per analysis to reduce the noise in the spectrum because some glasses have very low sulfur concentrations. We analyzed each glass in 4–6 locations preferably on different grains and the reference standards in at least 4 locations per minerals in each analytical session. Practically, the estimation of $[(\text{S}^{6+})/(\text{S}^{6+} + \text{S}^{2-})]$ was difficult for glasses containing < 100 ppm S; for example, the $[(\text{S}^{6+})/(\text{S}^{6+} + \text{S}^{2-})]$ could not be determined for the glasses of runs 1-08-04A, 1-08-04B, and 1-08-05A.

To estimate the oxidation state of S from the λ shifts in the S K_α X-rays, we calculated the rel% S^{6+} via Carroll and Rutherford (1988):

$$[(\text{S}^{6+})/(\text{S}^{6+} + \text{S}^{2-})] = 100 \times (\Delta\lambda(\text{SK}_\alpha)_{\text{sample}}/\Delta\lambda(\text{SK}_\alpha)_{\text{barite}}) \quad (1)$$

where

$$\Delta\lambda(\text{SK}_\alpha)_{\text{barite}} = \lambda(\text{SK}_\alpha)_{\text{barite}} - \lambda(\text{SK}_\alpha)_{\text{FeS}} \quad (2)$$

and

$$\Delta\lambda(\text{SK}_\alpha)_{\text{sample}} = \lambda(\text{SK}_\alpha)_{\text{sample}} - \lambda(\text{SK}_\alpha)_{\text{FeS}} \quad (3)$$

One calculates the apparent f_{O_2} of the melt:

$$\log[(X_{\text{S}^{6+}}^{6+})/(X_{\text{S}^{2-}}^{2-})] = a \log f_{\text{O}_2} + b/T + c \quad (4)$$

where $X_{\text{S}^{6+}}^{6+} = \%[(\text{S}^{6+})/(\text{S}^{6+} + \text{S}^{2-})]$ and $X_{\text{S}^{2-}}^{2-} = \%[(\text{S}^{2-})/(\text{S}^{6+} + \text{S}^{2-})]$ and $a = 1.02$, $b = 25,410$, and $c = -10.0$ (Wallace and Carmichael 1994). It should be noted that the dependence of $[(\text{S}^{6+})/(\text{S}^{6+} + \text{S}^{2-})]$ on f_{O_2} is quite sensitive; S speciation in melt varies significantly over a very small range in f_{O_2} (Jugo et al. 2010 and references cited therein).

Fourier-transform infrared spectroscopy

The concentrations of total H_2O (molecular water + hydroxyl) and CO_2 in the run-product glasses were determined with Fourier-Transform Infrared Spectroscopy (FTIR) at the AMNH (Table 1). Doubly polished chips of run-product glass were prepared, and their average thicknesses (e.g., 100–360 μm) were determined with a Mitutoyo digitometer (precision $\pm 2 \mu\text{m}$) taking 6–10 measurements per chip. The measurements were conducted at room temperature in transmittance mode using a Nicolet 20SXB FTIR spectrometer equipped with a Spectra Tech IR Plan microscope. Dry nitrogen gas was added at the rate of 15 l/min. IR spectra were collected both in the mid-IR (1,400–4,000 cm^{-1}) and near-IR (6,500–3,700 cm^{-1}) regions using a KBr beam splitter, a MCT/A detector, and a globar source. For each spectrum, 400 scans were performed and backgrounds were collected for each glass analyzed; the analytical resolution was 4 cm^{-1} . The height of each peak was measured from the baseline using

OMNIC software. Three to six analyses were collected in different spots of each polished glass chip, and these locations were selected to avoid vesicles in the path of the infrared beam. Due to the high total water concentrations in most glasses, the $3,550\text{ cm}^{-1}$ peak was nearly always saturated so in these cases the $4,500$ and $5,200\text{ cm}^{-1}$ peaks were used and the results combined to provide total H_2O concentrations. Molecular CO_2 was determined at the $2,349\text{ cm}^{-1}$ position, and the $1,550\text{ cm}^{-1}$ carbonate position was checked for several run-product glasses but no peaks were detected.

The volatile concentrations are related to the height of the absorbance peak by the Beer-Lambert law, which accounts for the density of the glass, molar absorptivity (i.e., the extinction coefficient) of the glass, as well as the thickness of the glass chips. Glass densities were calculated using the Gladstone-Dale rule (Gladstone and Dale 1864; Silver et al. 1990) and EPMA data; final values of glass densities were iteratively recalculated (at least twice) based on the apparent H_2O concentrations used in the first calculation. The associated precision is $\pm 0.03\text{ g/cm}^3$ according to Mandeville et al. (2002). The extinction coefficients that were used for the $5,200$ and $4,500\text{ cm}^{-1}$ peaks are 1.79 ± 0.02 and $1.56 \pm 0.02\text{ l cm}^{-1}/\text{mole}$ for H_2O and OH^- in rhyolitic glasses, respectively (Nowak and Behrens 1997). The absorption coefficient used for molecular CO_2 is $1,214 \pm 78\text{ l cm}^{-1}/\text{mole}$ for the $2,349\text{ cm}^{-1}$ peak in rhyolitic glasses (Behrens et al. 2004). Background subtraction was conducted with short tangential line segment approximations of the background. To test the accuracy of these analyses, two rhyolitic glasses—synthesized and originally analyzed by FTIR at the University of Hannover, Germany—were analyzed by FTIR at the AMNH. The total H_2O contents determined at Hannover for these glasses were 1.32 and 2.46 wt%, and our analyses gave 1.31 and 2.41 wt%, respectively.

Secondary ion mass spectrometry

The S concentrations of 13 felsic run-product glasses were determined with SIMS (Cameca 1,280 at the Woods Hole Oceanographic Institution) to serve as a comparison and test with the S concentrations determined by EPMA (Table 1). We also analyzed and compared data for several other hydrous, S-bearing granitic glasses not generated for this study, and all data are shown in Fig. 1. A primary beam of $^{133}\text{Cs}^+$ ions with currents between 1.0 and 1.5 nA was focused to a spot of $\sim 10\text{ }\mu\text{m}$ in diameter and rastered over a $30 \times 30\text{ }\mu\text{m}$ area, and a mechanical field aperture was placed at the position of the secondary ion image focal plane, such that only the central area of $15 \times 15\text{ }\mu\text{m}$ was analyzed. We used a normal-incidence electron gun to

compensate for the positive electrical charge deposited by the $^{133}\text{Cs}^+$ ion beam.

For each analytical cycle, the glasses were pre-cleaned by sputtering for a period of 4 min, secondary ion intensities of $^{30}\text{Si}^-$ and $^{32}\text{S}^-$ were measured, and this cycle repeated 10 times with a total analysis time of ~ 20 min. Intensity ratios of $^{32}\text{S}^-$ against $^{30}\text{Si}^-$ were averaged for 10 cycles. The NBS610 standard glass was analyzed 4 times, and a linear working curve was constructed through these data and the origin. This curve involves normalization of the $(^{32}\text{S}/^{30}\text{Si})$ for differences in bulk-silica content of the glasses and provides the calibration equation:

$$\text{concentration of S in glass (wt\%)} = 0.085 \times \left(\frac{^{32}\text{S}/^{30}\text{Si}}{\text{norm for Si}} \right) \quad (5)$$

Using these instrument conditions, prior work indicates a detection limit for S of at least 7 ppb (Rose-Koga in review). The agreement for S content between the EPMA and SIMS measurements is good. In addition, SIMS analyses accumulate tens of thousands of counts for S in a 5-second analysis of a glass containing several hundred ppm S, and with the number of S counts, $n = 10,000$, the $(n^{1/2}/n)$ estimate for precision based on count statistics gives 1% relative precision. This degree of precision contrasts with that determined by EPMA. For example, the total S counts range from 100 to 300 for glasses containing 100 to 600 ppm S, respectively, using the EPMA conditions described previously. With $n = 300$ S counts, the associated precision is 6 rel%, and with $n = 100$, the estimated precision for S by EPMA is 10 rel%, so the theoretical analytical variability for an individual analysis is considerably less for SIMS (summarized by Ripley et al. in press).

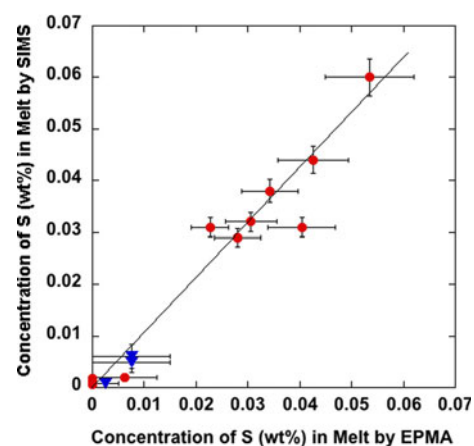


Fig. 1 Plot exhibiting good agreement between the sulfur concentration (wt%) of haplogranite run-product glasses of this study (circles) and other granitic glasses (triangles) measured by secondary ion mass spectrometry (SIMS) versus electron microprobe (EPMA). See text for description of “Methods”; precision shown is $1-\sigma$

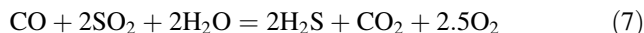
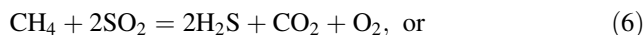
Estimating the fluid compositions

We assume that each experiment involved only one fluid phase in addition to silicate melt, and we computed the fluid composition at run conditions (Table 2) using the mass-balance approach of Webster (1992a, b) and Webster et al. (2009). This method involves computing the mass of the melt using the quantity of starting glass powder and accounting for the dissolution of H₂O, S, Na₂SO₄, and K₂SO₄ into the melt from the elemental S and fluids in the starting charge. It assumes that all S added to the starting charges dissolved in the melt and fluid. The mass of bulk fluid was calculated by accounting for the masses of H₂O, S, Na₂SO₄, and K₂SO₄ not sequestered by the melt and thus available for the fluid. The method also involves an iterative approach in computing the melt and fluid masses until the errors on bulk-system mass approach acceptable minima (i.e., when the observed change in fluid composition, between successive calculations, was <1 rel%).

Raman spectra of the dominant volatile-component species in the aqueous fluid-bearing vesicles of nine of the quenched, S-bearing run-product glasses were collected in the laboratory of Robert Bodnar at the Virginia Polytechnic Institute and State University (see Berkesi et al. 2009 for methods). Raman spectroscopy shows H₂O in all vesicles, and the fluid-bearing vesicles of seven of these run products contained CO₂. Six of the run-product glasses showed detectable H₂S in vesicles, and vesicles of two glasses showed measurable SO₂. None of the vesicles contained detectable CO or CH₄ at the estimated limit of detection of approximately one mol% (Robert Bodnar, personal communication).

The presence of CO and CH₄ in experimentally generated fluids can have a significant on volatile solubilities in melt at reducing f_{O_2} . A recent study of C–O–H fluids and haplobasaltic melts at 200–300 MPa and 1,250°C observed that the CO₂ solubilities in melt were reduced by the presence of CO and CH₄ in the fluid phase (Morizet et al. 2010). It is noteworthy that those experiments of Morizet et al. (2010) showing reduced CO₂ solubility in melt were conducted at relatively low $\log f_{O_2}$ (ca. NNO –3.2 to NNO –1.6), and that their runs at relatively higher f_{O_2} did not demonstrate this relationship. The lack of CO or CH₄ in the quenched run-product fluids in vesicles of our runs, determined by Raman analysis, suggests that neither of these species may have been present (at this limit of detection) at run conditions, but this argument assumes that no back reactions occur in the fluids during or after the quench. In this regard, Lin and Bodnar (2010) demonstrated that S-free, CH₄-bearing aqueous fluids can be quenched successfully without detectable CH₄ breakdown. Our run-product fluids, however, contained oxidized and reduced S species, and conceivably the reduction of SO₂ by

CO and/or CH₄ could consume these reduces C species during the quench, via:



Since we do not know if reactions like these consumed any CO and/or CH₄ that may, conceivably, have been present prior to the quench, we must rely on other evidence, discussed below, about the likelihood of these reduced C species in our relatively reduced runs.

To calculate fluid compositions, we have assumed that the only quantitatively significant C-bearing species in the fluid at run conditions was CO₂. Our experiments were conducted at significantly higher f_{O_2} and at significantly lower temperatures than those of Morizet et al. (2010). It has been demonstrated that the (CO/CO₂) of the fluid correlates with temperature (Holloway and Blank 1994), so the lower temperature runs of our study means that they were less likely to contain CO (than the runs of Morizet et al. 2010). Moreover, we calculated the maximum concentrations of CO and CH₄ in the fluids of our runs using PELE (available at: <http://www.nicholas.duke.edu/people/faculty/boudreau/Downloads.html>) for a COHS fluid in equilibrium with a felsic melt at the pressure–temperature conditions of our S-bearing runs. The maximum concentration of CO in these modelled fluids was 0.6 mol% with a molar (CO₂/H₂O) of 1.1 in the fluid and at $\log f_{O_2}$ of NNO –1.6 (below that of our runs), and was 0.3 mol% at $\log f_{O_2}$ of NNO with a molar (CO₂/H₂O) of 1.2. The CH₄ content of all of the modelled fluids was less than 0.01 mol% with $\log f_{O_2}$ of NNO –1.6 to NNO. Given that our S-bearing runs were conducted with the $\log f_{O_2}$ varying from NNO –0.4 to NNO + 1.4, the concentrations of CO and CH₄ are deemed negligible. In addition, it should be noted that the resulting data addressed herein do not account for the N₂ in the air present in the starting charge and capsule, but calculations by Tamic et al. (2001) estimate the $X_{N_2}^{\text{fluid}} < 0.04$ for experimental conditions similar to those of this study.

At present, there is no simple, readily available, and dependably accurate means of directly measuring the quantity of S in quenched run-product fluids (see summary in Webster and Botcharnikov in press). It is also worthy of mention that few prior experimental investigations have attempted to address the solubility behavior of H₂O, CO₂, and volatile S compounds in aluminosilicate melts simultaneously. Consequently, in order to evaluate the mass-balance calculations on these run fluids, we estimated the quantities of CO₂ ± other gaseous compounds and quantity of liquid H₂O in the run products at ambient conditions with the following gravimetric procedure. After each run, the exteriors of capsules were cleaned with reagent-grade alcohol and the capsule masses checked to confirm that the

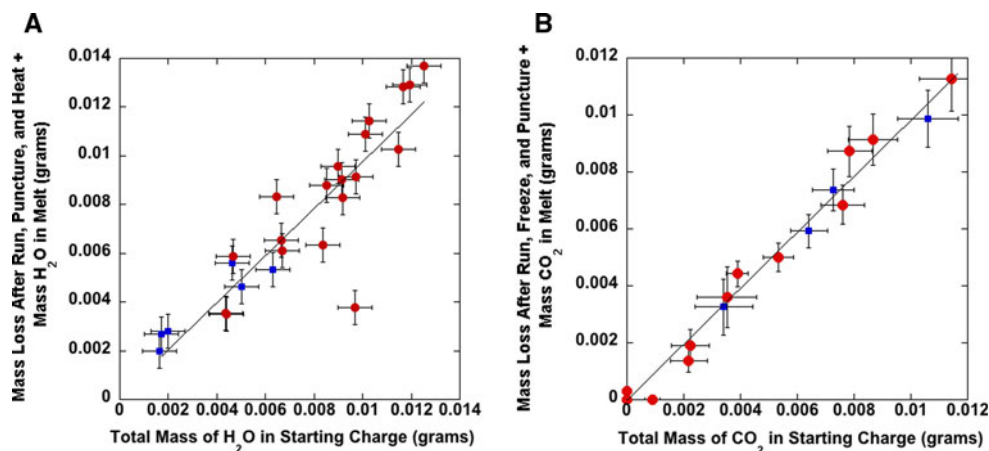


Fig. 2 Plot showing **a** the sum of the measured mass change after previously frozen and punctured run-product capsules of C–O–H–S-haplogranitic melt experiments were heated to 115°C (equivalent to mass of H₂O in run-product fluid) plus the mass of H₂O sequestered by the melt versus the total mass of H₂O added to the starting charge in the capsule. *Squares* represent C–O–H experiments and circles represent C–O–H–S runs. This comparison shows agreement for most experiments which is consistent with good analytical accuracy for H₂O in the glass, small weighing errors, and correct compositions of H₂O-bearing compounds in the starting charges. Plot **b** shows the sum

capsules had not lost volatiles by leakage during the experiment. Those capsules that had not leaked were cooled overnight to <−10°C in order to freeze the aqueous liquid still containing minor quantities of alkali sulfates, and the capsules were punctured and their masses recorded. The difference between the capsule mass after the run and the mass after the capsule freeze-and-puncture represents the quantity of CO₂ ± other volatile compounds (e.g., potentially H₂, SO₂, H₂S, SO₃) that did not solidify at the freezing temperature of salt-bearing H₂O and, hence, were released with the CO₂-dominated vapor when the capsule was punctured. Recall that the fluid of the S-bearing runs must contain some Na, K, and S as well as H₂O with or without dissolved CO₂. Subsequently, the opened capsules were heated to 115°C for at least 30 min, and the masses of the capsules recorded. This second mass difference (between that after the freeze and puncture and that after heating) represents the quantity of H₂O in the residual liquid that was vaporized from the capsule. These mass-difference measurements do not include the small quantity of volatiles trapped in fluid inclusions (vesicles in glass) nor the small masses of solid, residual Na₂SO₄ and K₂SO₄ in the heated run products. We note that trace coatings of salts were observed on the surfaces of run-product glass when the heated-and-dried capsules were subsequently cut open and the residual glass extracted for analysis.

In this regard, we have compared the total masses of H₂O and CO₂ added to the starting charges (based on the masses of compounds added to the capsules prior to

of the measured mass change after run-product capsules were frozen at <−10°C and punctured (equivalent to mass of CO₂ in run-product fluid) plus the mass of CO₂ sequestered by the melt versus the total mass of CO₂ added to starting charge. This step preceded the procedure described for **a**. This comparison shows good agreement for most experiments which is consistent with good analytical accuracy for CO₂ in the glass, small weighing errors, and correct compositions of CO₂-bearing compounds in the starting charges. See text for details on “**Methods**”; precision shown is 1−σ

welding) with these post-run gravimetric measurements (Fig. 2). Figure 2a compares the former value for H₂O with the sum of the mass-difference-measured-after-heating and the computed mass of H₂O in the run-product glass (based on the measured concentration of H₂O in the glass and the calculated mass of melt at run conditions). This latter value should be a good indication of the total quantity of H₂O in the run products (not accounting for the H₂O in vesicles/fluid inclusions), and the agreement is good for the great majority of the experiments. Similarly, the total mass of CO₂ added to the starting charges is compared with the sum of the mass-difference-after-freeze-and-puncture of the capsule and the computed mass of CO₂ in the run-product glass (Fig. 2b), and here the comparison is quite good. It should be noted this agreement also indicates that very little S was released as volatile compounds in vapor while the frozen capsule was punctured, and therefore, that most of the S was contained in the silicate glass and the frozen liquid portion of the run products. In other words, these measurements show that measurably little of the S in the run products occurred as SO₂, H₂S, or SO₃ in vapor and that S was largely contained by the frozen run-product liquid after the quench. We do note that some capsules emitted a strong H₂S odor when punctured.

Prior research on the behavior of S in high-temperature experiments indicates that S may be incorporated into gold capsules for run durations ≥120 h. Botcharnikov et al. (2004) observed that the distribution of S is heterogeneous in gold capsules after the runs are quenched, and they report that the maximum concentrations of S in the

capsules are <500 ppm. Conversely, Keppler (2010) ran tests with S-bearing, fluid-only runs in gold capsules to evaluate the extent of S loss to gold during experiments as long as 15 days, and he noted a small reduction in the S contents of the fluids but interpreted this change to difficulty in sampling the run-product fluids and not to loss of S to the gold capsules. Given the inherent difficulties associated with quantitatively estimating the quantity of S lost from the charges to the capsule material of our experiments, our calculations do not account for the potential loss of S to the capsules and, hence, the reported S concentrations of fluids may represent maximum values. Prior study (Mysen and Popp 1980) has also determined that the activity of S, a_S , in runs can be controlled or buffered by the presence of Me-MeS_x assemblages in which Me = Cu, Ag, or Pt. Hence, for run 1-08-05A it is likely that the a_S was controlled at some unconstrained value because of the presence of Ag (from the silver oxalate) and S (from the added Na₂SO₄ and K₂SO₄), and similarly for the Fe-bearing runs 1-10-15 A,B,C the a_S was likely modified by the reaction of Fe with reduced S. As a result, we report only the starting composition of the fluid for these runs (Table 2).

Results

The volatile-bearing run-product glasses are variably vesicular and are treated as compositionally equivalent to the melts in equilibrium with fluid at run conditions (Fig. 3). All experiments conducted, except for the three Fe-bearing runs and one unreported experiment, contain no crystals. The former runs include magnetite in the run products. The latter unreported run was conducted with a pure-CO₂ fluid, was crystal rich and melt poor, and hence, analysis of the glass was problematic. The molar (Al₂O₃/Na₂O + K₂O) ratio of the glasses ranges from 0.95 to 1.06 and the molar (Na₂O/Na₂O + K₂O) ranges from 0.55 to 0.61. These subtle compositional variations are due to the variable extraction of alkalis from the melt by S-bearing fluids (B. Evans, personal communication.; Webster et al. 2009; Beermann 2010).

The glasses contain ≤0.12 wt% S, ≤0.097 wt% CO₂, and ≤6.4 wt% H₂O. The abundances of S determined by SIMS agree well with the EPMA data (Fig. 1), and all references to the S contents of run-product glasses in the discussion that follow refer to S determined by EPMA. The $[(S^{6+})/(S^{6+}+S^{2-})]$ of these glasses ranges from 0.12 to 0.91, and the log f_{O_2} of most S-bearing runs computed for pressure of 200 MPa varies from NNO -0.4 to NNO + 1.4. It should be noted that recent modeling of sulfide-saturated rhyolitic melts at these P-T conditions (Moretti and Baker 2008) shows that the relationship involving f_{O_2}

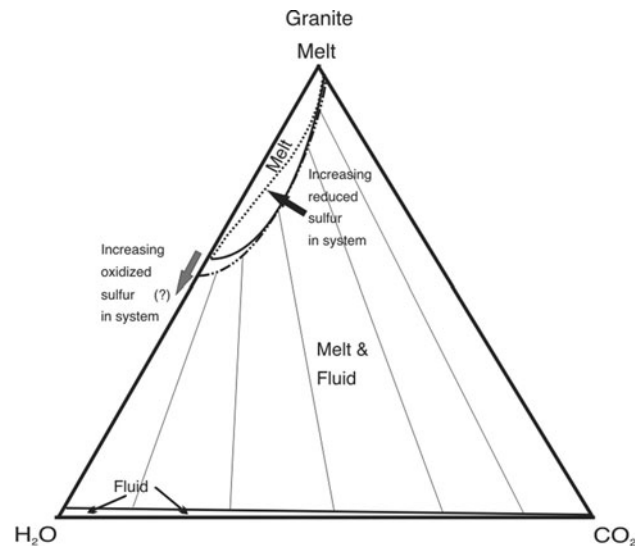


Fig. 3 Schematic representation of heterogeneous phase equilibria of this study of the pseudo-ternary system involving haplogranitic melt and C–O–H ± S-bearing fluids (expressed by tie lines shown as *faint straight curves*) projected on S-free basal plane for melt + H₂O + CO₂ based on 200-MPa molar abundances of volatiles in fluids and melt (i.e., [H₂O + CO₂]-bearing melt shown as *solid curves*, [H₂O + CO₂ + relatively oxidized S as *dot-dashed curve*], and [H₂O + CO₂ + relatively reduced S] as *dotted curve*). *Arrows* express the observed shift in the topological saturation surface for melt + COH-fluid with addition of reduced S to system and a potential shift in the saturation surface suggested by data of this study and indicated by those of Moretti and Baker (2008)

and $[(S^{6+})/(S^{6+}+S^{2-})]$ (Carroll and Rutherford 1988) varies with pressure and a_{H_2O} in the system, but we cannot account for the influence of changing a_{H_2O} on the apparent f_{O_2} values reported herein given that the a_{H_2O} of the melts is unconstrained.

Calculations show the fluids contained from ca. 10–99 wt% H₂O (22–99 mol%), 0–90 wt% CO₂ (0–78 mol%), 0–18 wt% S (0–12 mol%), and <3 wt% alkalis at 200 MPa and 900°C (Table 2). The associated volatile-solubility behavior in the felsic melt ranges from simple to complex (Fig. 4). For all S-free runs, the square of the mole fractions of H₂O of the glasses increases linearly with the modeled H₂O content of the fluid. Moreover, the H₂O contents of nearly all S-bearing glasses show greater dispersion (Fig. 4a). The solubility behavior of CO₂ in melt is more complex (Fig. 4b). For H₂O–CO₂-only runs and for the relatively oxidized C–O–H–S experiments having $[(S^{6+})/(S^{6+}+S^{2-})] \geq 0.4$, the molar concentration of CO₂ in the glasses increases with the modeled molar CO₂ content of the fluid and this correlation is quite robust. Comparison of these data with those for the relatively reduced S-bearing experiments having $[(S^{6+})/(S^{6+}+S^{2-})] < 0.4$, however, indicates that there is distinctly less CO₂ dissolved in these glasses for given concentrations of CO₂ in the S-bearing fluids. Thus, S dissolved primarily as S²⁻ in melt is associated with reduced

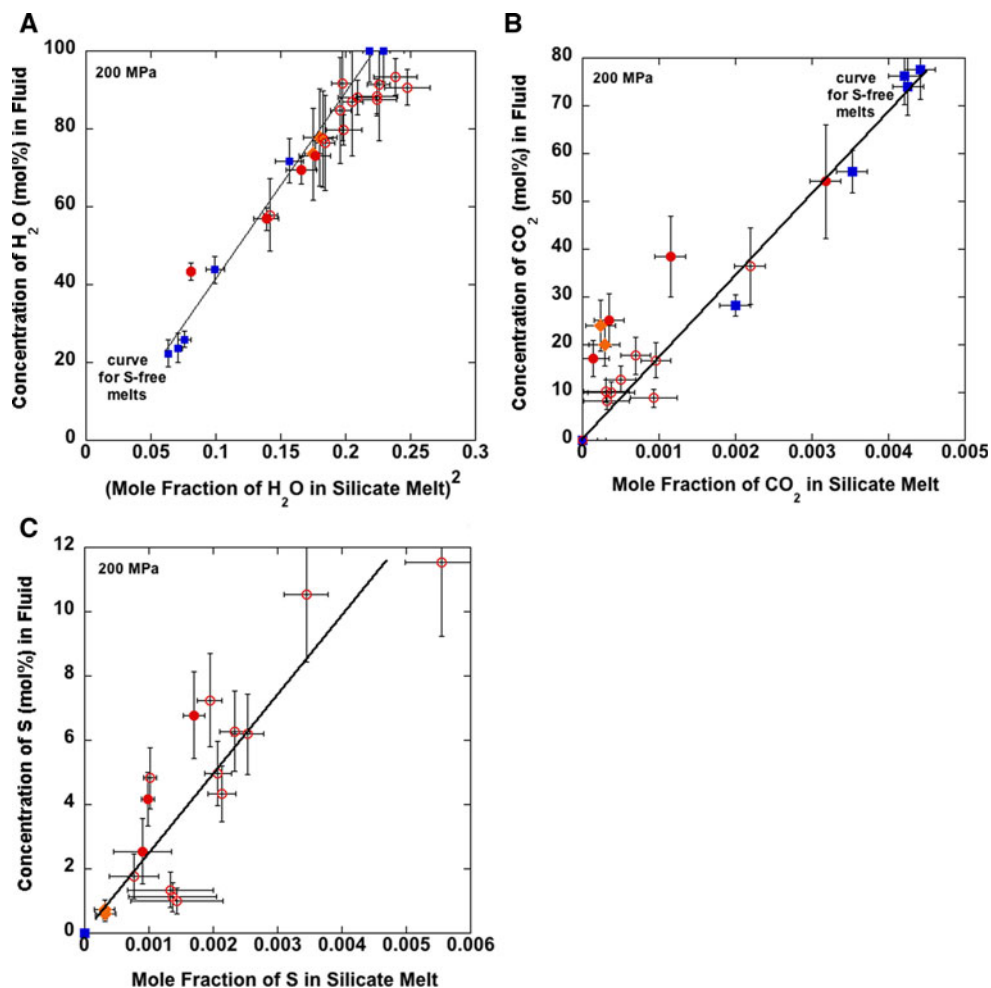


Fig. 4 Plot showing **a** the computed mol% H₂O of the fluid versus the square of the computed mole fraction of H₂O in haplogranitic melt ($X_{\text{H}_2\text{O}}^{\text{melt}})^2$ based on measured H₂O in run-product glass) at 200 MPa and 900°C. *Squares* represent C–O–H experiments, *solid diamonds* represent C–O–H–S runs at unconstrained f_{O_2} , *open circles* represent C–O–H–S runs at ca. $\log f_{\text{O}_2} > \text{NNO} + 0.3$, and *filled circles* show C–O–H–S runs at ca. $\log f_{\text{O}_2} \leq \text{NNO} + 0.3$. Data show that S-free C–O–H runs are consistent with linear increase in the $(X_{\text{H}_2\text{O}}^{\text{melt}})^2$ with increasing H₂O in the fluid, and the partitioning of H₂O between C–O–H–S fluid and melt is independent of the $(\text{S}/\text{S} + \text{CO}_2)$ of most runs. Plot **b** shows the computed mol% CO₂ of the fluid versus the

computed $X_{\text{CO}_2}^{\text{melt}}$ (based on measured CO₂ in run-product glass) at run conditions. Data show S-free runs are consistent with a linear increase in CO₂ concentration of melt with increasing CO₂ in the fluid, and the partitioning of CO₂ between fluid and melt is independent of the $(\text{S}/\text{S} + \text{CO}_2 + \text{H}_2\text{O})$ of most relatively oxidized runs. Plot **c** shows the computed S concentration of the fluid versus the computed $X_{\text{S}}^{\text{melt}}$ (based on measured S in run-product glass) at run conditions. Data show more dispersion than **(a)** or **(b)**, that most runs are consistent with increasing S in melt resulting from increasing S in fluid, and that the distribution of S between most melts and fluids does not vary detectably with $(\text{CO}_2/\text{CO}_2 + \text{H}_2\text{O})$. Precision shown is 1- σ

CO₂ contents of C–O–H–S fluid-saturated felsic melts. The behavior of S in melt is similar to that of H₂O, because increasing concentrations of S in the fluid cause increasing S in the melt (Fig. 4c), but the relationship for S exhibits greater dispersion than that shown for H₂O (Fig. 4a).

Discussion

Degassing of felsic magmas: volatile partitioning between C–O–H–S fluids and melt

The abundances of the primary volatile components C, H, and S and their ratios in pre-eruptive magmatic fluids and

eruptive volcanic gases provide important geochemical constraints on processes of degassing and information valuable for interpreting eruptive behavior, and our data represent results of the first experimental investigation of volatile dissolution behavior in C–O–H–S fluid-saturated felsic melts. The granitic-rhyolitic composition of the melts of this study is particularly relevant to volcanic processes because most explosive activity involves relatively evolved, silica-enriched, highly polymerized aluminosilicate melts (Cioni et al. 2000).

It is instructive to compare our experimental results with modeled and measured compositions of natural C–O–H–S-dominated fluids associated with felsic to

andesitic magmas of subduction-related and other volcanic environments (Table 2). Scaillet and Pichavant (2003) determined that the $X_{\text{H}_2\text{O}}^{\text{fluid}}$ ranges from 0.65 to 0.95, $X_{\text{CO}_2}^{\text{fluid}}$ ranges from 0 to 0.3, and that $X_{\text{S}}^{\text{fluid}}$ is typically <0.05 for the pre-eruptive vapor in magmas of these geologic environments (i.e., $X_{\text{S}}^{\text{fluid}}$ represents the sum of all sulfur species dissolved in the fluid in this discussion). These values are compatible with the ranges of the same parameters for most of our experiments. Eleven of our S-bearing runs have $X_{\text{S}}^{\text{fluid}} < 0.05$, four others have $X_{\text{S}}^{\text{fluid}}$ between 0.05 and 0.07, and the remaining two have $X_{\text{S}}^{\text{fluid}}$ of ca. 0.1–0.12. All but four experiments have $X_{\text{CO}_2}^{\text{fluid}} < 0.3$. Moreover, the range in $\log f_{\text{O}_2}$ for felsic to intermediate-silica magmas of these natural systems is ca. NNO -0.5 to NNO $+2$ (Scaillet and Pichavant 2003; Burgisser et al. 2008) which overlaps that of our experiments. In addition, if we compare the (C/S) ratios of the fluids of our experiments with those of these natural volcanic gases (Scaillet and Pichavant 2003, 2005), both sets of data are highly consistent with one another. Our results are also compatible with other constraints on natural systems. The atomic (C/S) ratios reported by Scaillet and Pichavant (2003, 2005) are consistent with the summary of Wallace and Edmonds (in press) in that the molar (C/S) of volcanic gases from volcanoes of arc environments tend to fall between 1 and 30. Our experimental molar (C/S) ranges from 0.8 to 34 (Table 2) and also shows that the bulk S content of the runs influences these parameters.

The experimentally determined fluid-melt partitioning behavior of these volatiles is also highly congruent with the modeled behavior for natural felsic to intermediate magmas (Fig. 5). The majority of these runs show similar correlations between increasing concentrations of CO_2 , S, and H_2O in the experimental fluids and increased CO_2 , S, and H_2O of the melts, respectively (Fig. 4), and these trends are captured by the distribution coefficients D_{CO_2} , D_{S} , and $D_{\text{H}_2\text{O}}$ expressing the partitioning of these volatile components between fluid and haplogranitic melt (reported in Table 2 and Fig. 5). Values of $D_{\text{H}_2\text{O}}$ are generally near 10, and they increase with increasing H_2O in the melt. This relationship implies that H_2O partitioning behavior is non-Nernstian, because H_2O partitions increasingly in favor of the fluid as the $X_{\text{H}_2\text{O}}$ of the system increases. D_{S} is generally an order-of-magnitude greater than $D_{\text{H}_2\text{O}}$ and shows greater variability, but D_{S} does not correlate with H_2O in the melt. The values of D_{CO_2} are generally an order-of-magnitude greater than those of D_{S} , exhibit no clear relationship with the H_2O content of the melt, and also show greater variability than $D_{\text{H}_2\text{O}}$. Moreover, the plots for D_{CO_2} and D_{S} involve outliers that differ significantly from the bulk of the data. The causes for the scatter involving D_{S} are undetermined, but they likely reflect the variability in oxygen fugacity and may also partially reflect the effect of

non-ideal mixing relationships for these volatiles in the melt and fluid. In comparison, Scaillet and Pichavant (2003) report apparent values of D_{CO_2} , D_{S} , and $D_{\text{H}_2\text{O}}$ that are based on the modeled fluid compositions described above and the volatile abundances of glasses in silicate melt inclusions from these systems. The general order: $D_{\text{CO}_2} > D_{\text{S}} > D_{\text{H}_2\text{O}}$ is expressed by both data sets, and the approximate order-of-magnitude difference between each partition coefficient is also supported. This general degassing sequence is consistent with other well-established observations on volcanic gases (Oppenheimer 2003).

At present, there are few experimental data detailing the partitioning of volatiles in C–O–H–S-bearing felsic systems, because most prior experiments only involved melt– H_2O – CO_2 or melt– H_2O –S. We do note that Gorbachev (1990) summarizes volatile solubilities for C–O–H–S-bearing basaltic and andesitic melts and Teague et al. (2008) report S partitioning data for C–O–H–S-bearing andesitic melt at 200–800 MPa. These studies reported that S is highly soluble in mixed CO_2 – H_2O fluids. In another experimental study, Parat et al. (2008) reacted andesite melt with C–O–H–S fluids at 400 MPa and observed that S modifies the proportions of H_2O and CO_2 in the melt as compared with S-free systems but they did not determine values of D_{S} .

Given the lack of appropriate experimental constraints for this system, it is instructive to revisit the partitioning

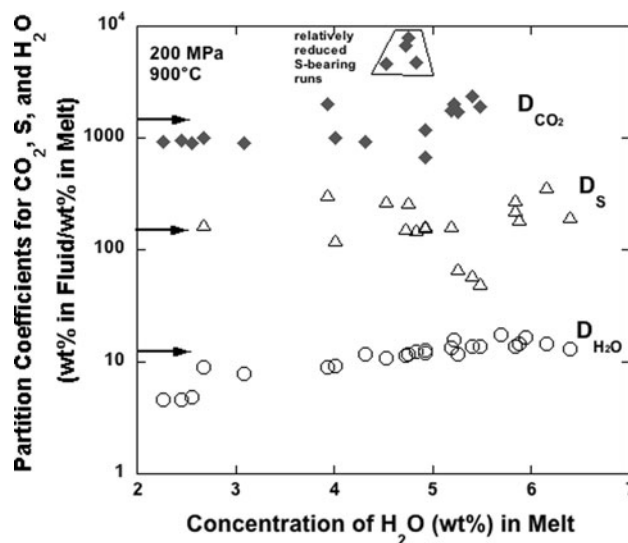


Fig. 5 Plots of the partition coefficients (wt% in C–O–H–S fluid/wt% in melt) for CO_2 (diamonds), S (triangles), and H_2O (circles) as a function of the H_2O concentration of haplogranitic melt at 200 MPa and 900°C showing $D_{\text{CO}_2} > D_{\text{S}} > D_{\text{H}_2\text{O}}$. $D_{\text{H}_2\text{O}}$ increases with increasing H_2O in the melt, but D_{CO_2} and D_{S} show no clear relationship with H_2O content of melt. Arrows designate the relative partitioning behavior of these volatile components in natural pre-eruptive magmatic fluids of subduction-related magmas and magmas of other tectonic environments characterized by Scaillet and Pichavant (2003); the experimental data agree with those characterizing natural systems

behavior for H₂O, CO₂, and S between fluid and haplogranitic melt (Figs. 4, 6). Figure 4a compares the H₂O concentrations of our S-free haplogranitic melts with the H₂O concentrations of S-bearing haplogranitic melts at 200 MPa. The latter data show a linear increase in the $(X_{\text{H}_2\text{O}}^{\text{melt}})^2$ with increasing H₂O in the fluid that is statistically consistent with our S-free runs, at the 1- σ level of precision. It is noteworthy that several of the S-bearing runs involving the most H₂O-enriched fluids, i.e., those with the least CO₂ and with $(X_{\text{H}_2\text{O}}^{\text{melt}})^2 > 0.22$, suggest comparatively elevated solubility of H₂O in melt compared with S-free melts. This solubility relationship was observed previously in modeling of Moretti and Papale (2004) which predicts that the 200-MPa solubility of H₂O in rhyolitic melt increases by ca. 0.3 wt% as the $(f_{\text{SO}_2}/f_{\text{H}_2\text{S}})$ increases from 0.1 to 10 (at 827°C). Although this apparent difference in H₂O solubility behavior (Fig. 4a) is not statistically valid, it is consistent with prior results and deserves additional experimental study.

We also compare the partitioning of CO₂ between melts and fluids of our runs with that of the S-free experiments of Liu et al. (2005) for rhyolitic melts at 200 MPa and 900°C (Fig. 6a), and the $X_{\text{CO}_2}^{\text{melt}}$ increases with increasing abundances of CO₂ in the coexisting C–O–H fluid for both data sets. Prior investigations involving felsic melts have either observed or assumed the CO₂–H₂O mixing behavior in the fluid to be fit with a linear curve (i.e., expressing ideal behavior) for S-free conditions and pressures ≤ 200 MPa (Blank et al. 1993; Newman and Lowenstern 2002; see summary of Moore 2008). In this context, most of our

S-free runs and most of our relatively oxidized S-bearing runs are consistent, within precision, with a linear mixing curve for the fluid and Henrian-solubility behavior for CO₂ in melt. Conversely, particularly strong curvature—that expresses the dramatic reduction in the CO₂ concentration of these felsic melts—is associated with the addition of S at $f_{\text{O}_2} \leq \text{NNO} + 0.3$ and with < 50 mol% CO₂ in the fluid.

The equilibrium distribution of S between granite melt and C–O–H–S fluids shows significant dispersion that precludes robust interpretation of the mixing behavior in fluid and the corresponding solubility behavior in melt (Fig. 6b). Sulfur partitioning does vary with f_{O_2} as reported previously for C-free granitic systems (Scaillet et al. 1998; Keppler 1999; Scaillet and Pichavant 2003, 2005; Clemente et al. 2004; Keppler 2010), but it does not vary with the $(\text{CO}_2/\text{CO}_2 + \text{H}_2\text{O})^{\text{fluid}}$. Our data are compared in Fig. 6b with the partitioning behavior of S for O–H–S fluids and haplogranitic melts at 200 MPa and 850°C with f_{O_2} equal to that of the Co–CoO buffer and also in the range of ca. NNO + 0.5 to NNO + 1 log units (Keppler 1999, 2010). Even though our data exhibit significant scatter, the S contents of fluid and coexisting melt for our C-free experiments are consistent with those of our C-bearing runs, so D_{S} is indeed independent of $(\text{CO}_2/\text{CO}_2 + \text{H}_2\text{O})^{\text{fluid}}$ with felsic melts at these conditions. Thus, sulfur solubility in aqueous fluids is similar to that in aqueous-carbonic fluids at 200 MPa. This relationship has important implications for S degassing, since CO₂ shows the strongest partitioning in favor of fluid (Fig. 5), and hence, CO₂-

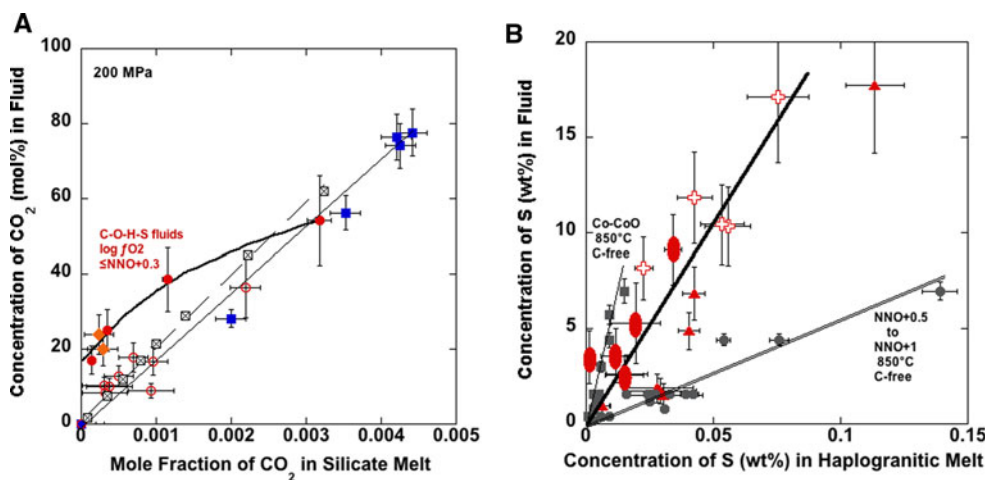


Fig. 6 Plots showing experimental results at 200 MPa and 900°C of this study **a** mol% CO₂ in fluid versus the mole fraction of CO₂ in melt for S-free, H₂O–CO₂ fluids (filled squares fit by fine solid line), O–H–S ± C fluids with unconstrained f_{O_2} (filled diamonds), O–H–S ± C fluids with $\log f_{\text{O}_2} > \text{NNO} + 0.3$ (open circles), O–H–S–C fluids with $\log f_{\text{O}_2} \leq \text{NNO} + 0.3$ (filled circles fit by bold solid curve), and—for comparison—squares containing x’s represent modeled data for S-free, C–O–H runs of Liu et al. (2005) fit by dashed line. Plot **b** shows wt% S in C–O–H–S fluids versus wt% S in

haplogranite melts of this study fit by bold line compared with S distribution between O–H–S fluid and haplogranite melt (at 200 MPa, 850°C, and $\log f_{\text{O}_2}$ equivalent to Co–CoO buffer [filled squares fit by fine line] and $\log f_{\text{O}_2}$ in range of NNO + 0.5 to NNO + 1 [filled circles fit by double line] of [Keppler 2010]). Open crosses represent S-free, C–O–H runs of this study, triangles represent C–O–H–S runs of this study with $\log f_{\text{O}_2} > \text{NNO} + 0.3$ or unconstrained, and ellipses show O–H–S–C runs of this study with $\log f_{\text{O}_2} \leq \text{NNO} + 0.3$. Precision shown is 1- σ

enriched fluid tends to exsolve earlier (Holloway 1987) and deeper than other volatiles during magma ascent and evolution in the crust. It follows that $\text{H}_2\text{O} + \text{CO}_2$ fluids are likely to exhibit a significant capacity to dissolve and carry S at higher pressures (Oppenheimer 2003), and this is consistent with current experimental research for mafic and intermediate magmas (Teague et al. 2008; Lesne et al. in press). Interestingly, the bulk of our data lie between and show some consistency with Keppler's (2010) data for S-free runs. Our relatively oxidized runs lie near Keppler's $\text{NNO} + 0.5$ to $\text{NNO} + 1$ runs, and our four most-reduced runs lie nearer to the Co–CoO curve of Keppler (2010). These associations indicate a generally consistent distribution of S between melts plus aqueous fluids and melts plus aqueous-carbonic fluids as a function of apparent f_{O_2} (even though the f_{O_2} constrained from the $[(\text{S}^{6+})/(\text{S}^{6+} + \text{S}^{2-})]$ of some of our glasses may involve significant error).

Sulfur and CO_2 and H_2O solubility in felsic melt

It is well established from prior experimental investigations (Holloway 1987; Fogel and Rutherford 1990; Holloway and Blank 1994; Botcharnikov et al. 2005; Moore 2008 and references therein) that the dissolution of H_2O and CO_2 in fluid-saturated granitic melts varies with pressure and the $(\text{H}_2\text{O}/\text{H}_2\text{O} + \text{CO}_2)^{\text{fluid}}$. Currently, there are multiple sets of FTIR extinction coefficients for the analysis of H_2O and CO_2 and multiple solubility models for these components in felsic glasses and melts, respectively. We analyzed the seven 900° S-free haplogranite glasses using the extinction coefficients of Behrens et al. (2004) for CO_2 and Nowak and Behrens (1995) for H_2O and OH^- (Fig. 7). The measured H_2O and CO_2 concentrations of the run-product glasses are compared with modeled solubilities of these volatiles in S-free rhyolitic melt at 100–200 MPa (Newman and Lowenstern 2002), and the two data sets correspond well with one another. This consistency suggests that the IHPV quench rate and the FTIR analyses for H_2O and CO_2 in this investigation were adequate.

The other experiments show that the concentration of CO_2 in O–H–S \pm C-bearing fluid-saturated haplogranite melts varies with the S concentration of the system and f_{O_2} (Figs. 7, 8a). The presence of S, dissolved in melt largely in the reduced state, decreases the volatile saturation pressure for C–O–H–S-bearing melts relative to that of C–O–H-bearing melts and that of S-bearing melts at relatively oxidizing conditions (Fig. 7). For most S-bearing runs with $[(\text{S}^{6+})/(\text{S}^{6+} + \text{S}^{2-})]_{\text{glass}} < 0.4$, the 200-MPa H_2O and CO_2 concentrations of melt are located nearer to those of the 150-MPa C–O–H volatile solubility curve of Newman and Lowenstern (2002). This contrasts with the apparent influence of oxidized S on CO_2 solubilities.

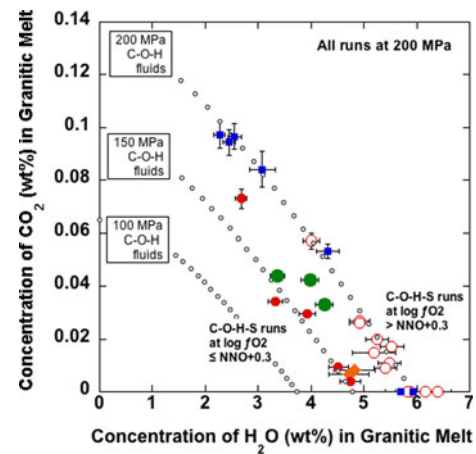


Fig. 7 Plot showing experimental results at 200 MPa and 900°C of this study and comparing the wt% CO_2 in C–O–H–S fluid-saturated haplogranite and Fe-bearing haplogranitic melt versus the wt% H_2O in same melts; symbols are the same as in Fig. 6 for runs with haplogranite melt except for three iron-bearing “haplogranitic” melts shown as large filled circles. Experimental data are compared with computed CO_2 and H_2O concentrations of vapor-saturated rhyolite melt at 900°C and 200, 150, and 100 MPa (fine crosses) based on modeling of Newman and Lowenstern (2002). The presence of >0.02 wt% S in melt and >3 wt% S in fluid (with $\log f_{\text{O}_2} \leq \text{NNO} + 0.3$) reduce CO_2 solubilities in 200-MPa melts to values approximately equivalent to those for S-free, C–O–H-fluid-saturated melts at 150 MPa. Precision shown is $1-\sigma$; see text for “Discussion”

This solubility relationship has important implications for geobarometric interpretation of the pressures of melt inclusion entrapment and for degassing behavior of C–O–H–S-bearing magmas. This application of H_2O and CO_2 solubilities is reviewed for S-free conditions by Moore (2008), Métrich and Wallace (2008), and references cited therein. A detailed discussion of this approach is out of scope for this investigation, but nevertheless our results for felsic melts imply that the determination of C–O–H–S solubilities for basaltic and intermediate-silica content melts should be expanded to cover a broad range of crustal pressures and temperatures (i.e., beyond the initial results of Gorbachev (1990) and Teague et al. (2008)).

Thermodynamic considerations on volatile mixing in C–O–H–S fluid-saturated melts

In systems involving heterogeneous fluid-melt equilibria, the activities of volatile components in fluid-saturated silicate melts are influenced by the concentrations of the volatiles in coexisting fluid(s) and by the ideal versus non-ideal nature of volatile mixing in the melt and fluid. For instance, increasing the abundance of CO_2 in an aqueous fluid will reduce the $X_{\text{H}_2\text{O}}^{\text{fl}}$ and $X_{\text{H}_2\text{O}}^{\text{melt}}$ by dilution and will, likewise, reduce the $a_{\text{H}_2\text{O}}^{\text{fl}}$ and $a_{\text{H}_2\text{O}}^{\text{melt}}$ as long as there is negligible non-ideal mixing behavior in the fluid (i.e., γ_{CO_2} and $\gamma_{\text{H}_2\text{O}}$ change little during mixing). At 200 MPa and

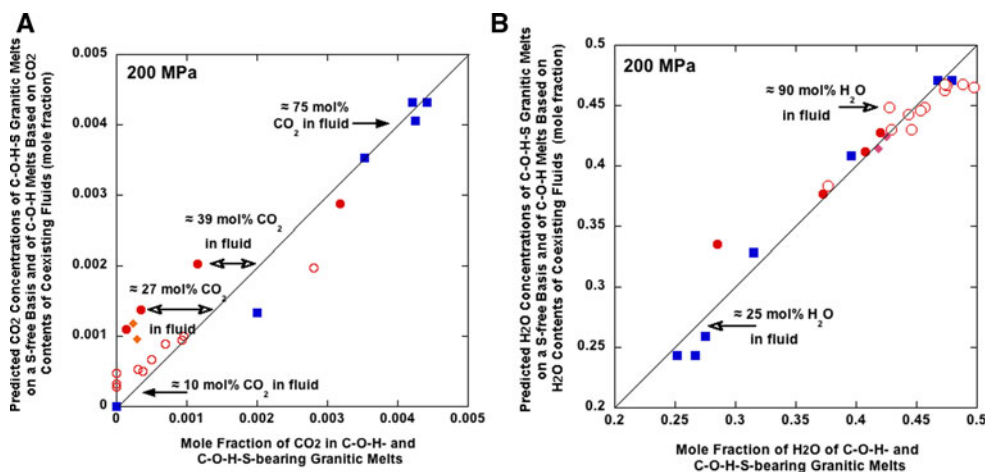


Fig. 8 Plots comparing a predicted mole fraction of CO₂ in C–O–H melts and C–O–H–S melts, on a S-free basis, versus the measured mole fraction of CO₂ in all melts at 200 MPa and 900°C, and b predicted mole fraction of H₂O in C–O–H melts and C–O–H–S melts, on a S-free basis, versus the measured mole fraction of H₂O in all melts at 200 MPa and 900°C for C–O–H ± S fluids (symbols same as in Fig. 6). Predicted CO₂ and H₂O concentrations derived from

900°C for example, H₂O and CO₂ exhibit small positive deviations from ideal mixing with S-free fluids (Kerrick and Jacobs 1981); the model of Aranovich and Newton (1999) indicates, with $X_{\text{H}_2\text{O}}^{\text{fl}}$ and $X_{\text{CO}_2}^{\text{fl}}$ of 0.5, that the $a_{\text{H}_2\text{O}}^{\text{fl}}$ is 0.56 and the $a_{\text{CO}_2}^{\text{fl}}$ is 0.538.

A detailed analysis of the S-bearing fluids and coexisting melts of the present study provides additional constraints on volatile dissolution behavior. The shift in the volatile concentrations of the melts as a function of increasing reduced S²⁻ in the melt, for example, is due primarily to reduced CO₂ in the melt; the presence of reduced S in the system does not appear to alter the solubility of H₂O (Fig. 8a). This graph compares the measured CO₂ contents of the C–O–H melts with predicted values of CO₂ in melt that account for the effects of dilution by H₂O. For these S-free runs, we used the computed CO₂ concentrations of the fluids and the volatile solubility data of Liu et al. (2005) to model the CO₂ solubility in rhyolite melt at 200 MPa and 900°C. This accounts for dilution of CO₂ in the fluid-melt system, by the addition of H₂O to the starting charges, using the general solubility model of Liu et al. (2005) that is based on experiments covering a range of pressure and temperature. Figure 8a also compares the measured CO₂ contents of the C–O–H–S melts with the predicted CO₂ in melt for the C–O–H–S melts on a S-free basis. For this comparison, we summed the number of moles of S (i.e., total S) in the fluid with the number of moles of H₂O in the fluid in order to reduce the moles of CO₂ in the fluid, and then employed this modified fluid composition and the volatile solubility data of Liu et al. (2005) to model the corresponding CO₂ solubility in the

experiments and volatile solubility model of Liu et al. (2005) for S-free experiments at 200 MPa and 900°C as described in text. Arrows in a show range in fluid composition (e.g., mol% CO₂) and allow comparison of predicted CO₂ in melt for S-bearing and S-free runs. Arrows in b show fluid composition (e.g., mol% H₂O) and allow comparison of predicted H₂O in melt for S-bearing and S-free runs

melt. This approach treats each mole of S in fluid as equivalent to one mole of H₂O in fluid, with regard to their capacity to dilute the CO₂ in the system. This comparison shows that the predicted CO₂ contents of the melts in the majority of the S-free runs and in the comparatively oxidized S-bearing runs are equivalent to their measured CO₂ concentrations. Conversely, the measured CO₂ contents of three of the relatively reduced S-bearing melts and the two S-bearing melts with unconstrained f_{O_2} are significantly less than those predicted for these melts on a sulfur-free basis (i.e., calculated as if in equilibrium with C–O–H-only fluids). This difference reflects the influence of reduced S in fluid-saturated systems on CO₂ dissolution in melt.

The corresponding graph of measured versus predicted H₂O in the melts (Fig. 8b) shows that the H₂O contents of melts of the S-bearing runs (whether relatively oxidized or reduced) as well as those of the S-free, C–O–H-bearing melts either fit or lie near the 1:1 correspondence curve. In fact, except for a single outlier involving a relatively reduced S-bearing melt, the data show remarkable consistency. This general agreement implies that each mole of CO₂ in the fluid behaves similarly to that of the moles of oxidized and reduced S species in the fluid with regard to dilution of H₂O, and at these conditions, the S in fluid should occur primarily as SO₂ plus sulfide, and potentially, sulfate species (Carroll and Webster 1994). These data also confirm that the observed changes in volatile solubility (i.e., the shifts in the 200-MPa data in Fig. 7 toward the 150-MPa solubility curve) are primarily the result of changing CO₂ concentrations with little modification of the H₂O contents.

Theoretically, the addition of S to the mixed H₂O- and CO₂-bearing fluids of these experiments should reduce the $X_{\text{H}_2\text{O}}^{\text{fl}}$ and the $X_{\text{CO}_2}^{\text{fl}}$ by dilution (Fig. 4) just as the addition of CO₂ to the fluid reduces the H₂O concentration of the melt (the $(X_{\text{H}_2\text{O}}^{\text{melt}})^2$ decreases in a linear fashion with the $X_{\text{H}_2\text{O}}^{\text{fl}}$ for a decrease in the mol% H₂O in the fluid). Recall that the H₂O and CO₂ concentrations of these fluids were diluted with as much as 12 mol% S. This behavior has been observed in prior research; for example, in hydrothermal experiments involving andesite melt–C–O–H–S (Parat et al. 2008). The addition of S to their 400-MPa runs reduced the $X_{\text{H}_2\text{O}}^{\text{melt}}$, because the estimated H₂O concentrations of the S-bearing run-product glasses were lower than those of the corresponding S-free runs for given amounts of H₂O and CO₂ in the system. We can compare, quantitatively, the relative effects of dilution by CO₂ versus S in the fluids of our runs. The slope of the curve fitting the S-free runs (Fig. 4a) is:

$$\text{mol\% H}_2\text{O in aqueous fluid} = (-6.596) + (480.1) \times (X_{\text{H}_2\text{O}}^{\text{melt}})^2 \quad (8)$$

and solving this equation for the change in $X_{\text{H}_2\text{O}}^{\text{melt}}$ when the H₂O content of a S-free aqueous fluid is diluted by the addition of 10 mol% CO₂ (i.e., which is arbitrarily chosen to be less than the maximum S content computed for the fluids of these experiments) gives the result that the $X_{\text{H}_2\text{O}}^{\text{melt}}$ is reduced by a factor of 0.023 (equivalent to a reduction of 0.25 wt% H₂O in the melt). The apparent mixing behavior of CO₂ in C–O–H–S fluid–melt systems is not as easily interpreted. The relatively oxidizing experiments show (Figs. 4b, 6a) that values of the $X_{\text{CO}_2}^{\text{melt}}$ are consistent, within precision, with those determined in our S-free runs and with values predicted for CO₂ partitioning between S-free melts and fluids at this pressure (Liu et al. 2005). Given the dispersion in the oxidized experiments, one cannot readily interpret the responses of $\gamma_{\text{CO}_2}^{\text{fl}}$ and $\gamma_{\text{CO}_2}^{\text{melt}}$ as a function of increasing S in the fluid with confidence given the inherent imprecision in the computed fluid compositions. Conversely, the addition of S to relatively reduced C–O–H fluids has a distinct influence by strongly reducing $X_{\text{CO}_2}^{\text{melt}}$.

Interpretation of the influence of the mixing relationships in these C–O–H–S fluids and melts on S solubility is problematic given the strong influence of f_{O_2} (Fig. 6b) on S solubility in silicate melts (Clemente et al. 2004; Keppler 2010). Any potential influence of the (CO₂/CO₂ + H₂O) of our runs on the $X_{\text{S}}^{\text{melt}}$ is overridden by the variable f_{O_2} . This problem is exacerbated by the fact that precise control of f_{O_2} in experimental apparatus requires control and knowledge of the $a_{\text{H}_2\text{O}}$, but for these mixed C–O–H–S fluids and melts we have poor constraints on the f_{S_2} and $\gamma_{\text{H}_2\text{O}}$ and hence on $a_{\text{H}_2\text{O}}$. Our data do imply that S solubility in C–O–H–S-bearing haplogranitic melt is generally similar to that

in O–H–S-bearing granite melt, but our data also show significant dispersion. Some of the dispersion in S partitioning correlates with the apparent f_{O_2} of the runs and is consistent with the reported change in S partitioning between haplogranite melt and O–H–S-bearing fluids with $\log f_{\text{O}_2}$ of Co–CoO and NNO + 0.5 to NNO + 1 (Keppler 2010). We do note that the MRK modeling of Clemente et al. (2004) predicts greater non-ideal mixing behavior for SO₂ than H₂S, that H₂S appears to be more soluble in felsic melts than SO₂ (at equivalent $f_{\text{H}_2\text{S}}$ and f_{S_2}), and that H₂S solubility should follow Henry's law at conditions like those of our experiments. Clearly, however, additional volatile solubility research—at carefully defined values of f_{O_2} —is called for.

Summary

This investigation provides the first systematic, experimental data set that constrains H₂O, CO₂, and S solubility and partitioning behavior for C–O–H–S fluids and felsic melt at oxygen fugacities that are geologically relevant to high-silica rhyolitic magmas and some subduction-related, calc-alkaline magmatic systems (Scaillet and Pichavant 2003). In short, the presence of S, largely as reduced S²⁻ in melt, lowers the solubility of CO₂ in felsic melt at 200 MPa. Interestingly, recent modeling of the ascent of rhyolitic magma saturated in H–O–S gas from 200 MPa to the surface (Burgisser and Scaillet 2007) indicates that the $\log f_{\text{O}_2}$ of a S-bearing magma initially at NNO –0.5 will increase slightly and subsequently decrease—potentially to values as low as NNO –1 if the initial gas content approaches 5 wt%. It follows that the solubility and partitioning behavior of C–O–H–S volatiles will be quite complex during the ascent of fluid-saturated magma as pressure decreases, f_{O_2} varies, and CO₂ solubility in melt varies. Given the observed influence of oxidized and reduced S on H₂O and CO₂ solubilities in felsic melt, future experiments should search for similar relationships for felsic melts at other pressures and for intermediate and mafic melts at shallow crustal pressures. Finally, particularly important issues that are yet-to-be-resolved include: what controls f_{S_2} in natural systems and how does iron affect S partitioning?

Acknowledgments We appreciate thoughtful reviews by Editor Tim Grove and two anonymous referees. We also wish to recognize discussions on analytical methods with Charles Mandeville. Our thanks are offered to Professor David London of the University of Oklahoma who provided the haplogranite starting glass and Professor Harald Behrens of the University of Hannover, Germany, who provided two synthetic glasses with measured H₂O contents that were used to test our FTIR analyses. Robert Bodnar and Charles Farley, of Virginia Tech, kindly conducted Raman analyses of 9 of the run-

product glasses to determine the dominant volatile species in the vesicles. This research was supported in part by National Science Foundation awards EAR 0308866 and EAR-0836741 to J.D.W.

References

- Aranovich LY, Newton RC (1999) Experimental determination of $\text{CO}_2\text{-H}_2\text{O}$ activity-composition relations at 600–1000°C and 6–14 kbar by reversed decarbonation and dehydration reactions. *Am Miner* 84:1319–1332
- Beermann O (2010) The solubility of sulfur and chlorine in H_2O -bearing dacites of Krakatau and basalts of Mt. Etna. Dissertation, University of Hannover, 109 p
- Behrens H, Tamic N, Holtz F (2004) Determination of the molar absorption coefficient for the infrared absorption band of CO_2 in rhyolitic glasses. *Am Miner* 89:301–306
- Berkesi M, Hidas K, Guzmics T, Dubessy J, Bodnar RJ, Szabo C, Vajna B, Tsunogae T (2009) Detection of small amounts of H_2O in CO_2 -rich fluid inclusions using Raman spectroscopy. *J Raman Spectrosc* 40:1461–1463
- Blank JG, Stolper EM, Carroll MR (1993) Solubilities of carbon dioxide and water in rhyolitic melt at 850°C and 750 bars. *Earth Planet Sci Lett* 119:27–36
- Botcharnikov RE, Behrens H, Holtz F, Koepke J, Sato H (2004) Sulfur and chlorine solubility in Mt. Unzen rhyodacite melt at 850°C and 200 MPa. *Chem Geol* 213:207–225
- Botcharnikov RE, Freise M, Holtz F, Behrens H (2005) Solubility of C-O-H mixtures in natural melts: new experimental data and application range of recent models. *Ann Geophys* 48:633–646
- Burgisser A, Scaillet B (2007) Redox evolution of a degassing magma rising to the surface. *Nature* 445:194–197
- Burgisser A, Scaillet B, Harshvardhan (2008) Chemical patterns of erupting silicic magmas and their influence on the amount of degassing during ascent. *J Geophys Res* 113(B12204):14
- Carroll MR, Rutherford MJ (1988) Sulfur speciation in hydrous experimental glasses of varying oxidation state: results from measured wavelength shifts of sulfur X-rays. *Am Min* 73:845–849
- Carroll MR, Webster JD (1994) Solubilities of sulfur, noble gases, nitrogen, chlorine, and fluorine in magmas. *Rev Miner* 30:231–279
- Cioni R, Marianelli P, Santacroce R, Sbrana A (2000) Plinian and subplinian eruptions. In: Sigurdsson H (ed) *Encyclopedia of volcanoes*. Academic Press, San Diego, pp 477–494
- Clemente B, Scaillet B, Pichavant M (2004) The solubility of sulphur in hydrous rhyolitic melts. *J Petrol* 45:2171–2196
- Fogel RA, Rutherford MJ (1990) The solubility of carbon dioxide in rhyolitic melts: a quantitative FTIR study. *Am Miner* 75:1311–1326
- Gladstone JH, Dale TP (1864) Researches on the refraction, dispersion, and sensitiveness of liquids. *Phil Trans R Soc London* 153:317–343
- Gorbachev NS (1990) Fluid-magma interaction in sulfide-silicate systems. *Int Geol Rev* 32:749–836
- Holloway JR (1987) Igneous fluids. *Rev Miner* 17:211–232
- Holloway JR, Blank J (1994) Application of experimental results to C-O-H species in natural melts. *Rev Miner* 30:187–230
- Jugo P, Wilke M, Botcharnikov RE (2010) Sulfur K-edge XANES analysis of natural and synthetic basaltic glasses: implications for S speciation and S content as function of oxygen fugacity. *Geochim Cosmochim Acta* 74:5926–5938
- Keppeler H (1999) Experimental evidence for the source of excess sulfur in explosive volcanic eruptions. *Science* 284:1652–1654
- Keppeler H (2010) The distribution of sulfur between haplogranitic melts and aqueous fluids. *Geochim Cosmochim Acta* 74:645–660
- Kerrick DM, Jacobs GK (1981) A modified Redlich-Kwong equation for H_2O , CO_2 , and $\text{H}_2\text{O-CO}_2$ mixtures at elevated pressures and temperatures. *Am J Sci* 281:735–767
- Lesne P, Kohn SC, Blundy J, Witham F, Botcharnikov RE, Behrens H (in press) Experimental simulation of basalt degassing at Stromboli and Masaya volcanoes. *J Petrol*
- Lin B, Bodnar RJ (2010) Synthetic fluid inclusions XVIII: experimental determination of the PVTX properties of $\text{H}_2\text{O-CH}_4$ to 500°C, 3 kbar and $X_{\text{CH}_4} \leq 4$ mol%. *Geochim Cosmochim Acta* 74:3260–3273
- Liu Y, Zhang Y, Behrens H (2005) Solubility of H_2O in rhyolitic melts at low pressures and a new empirical model for mixed $\text{H}_2\text{O-CO}_2$ solubility in rhyolitic melts. *J Volcanol Geotherm Res* 143:235–291
- Mandeville CW, Webster JD, Rutherford MJ, Taylor BE, Timbal A, Faure K (2002) Determination of molar absorptivities for infrared absorption bands of H_2O in andesitic glasses. *Am Min* 87:813–821
- Matthews SJ, Moncrieff DHS, Carroll MR (1999) Empirical calibration of the sulphur valence oxygen barometer from natural and experimental glasses; method and applications. *Miner Mag* 63(3):421–431
- Métrich N, Clocchiatti R (1996) Sulfur abundance and its speciation in oxidized alkaline melts. *Geochim Cosmochim Acta* 60:4151–4160
- Métrich N, Wallace PJ (2008) Volatile abundances in basaltic magmas and their degassing paths tracked by melt inclusions. *Rev Mineral Geochem* 69:363–402
- Moore G (2008) Interpreting H_2O and CO_2 contents in melt inclusions: constraints from solubility experiments and modeling. *Rev Mineral Geochem* 69:333–361
- Moretti R, Baker DR (2008) Modeling the interplay of f_{O_2} and f_{S_2} along the FeS-silicate melt equilibrium. *Chem Geol* 256:286–298
- Moretti R, Papale P (2004) On the oxidation state and volatile behavior in multicomponent gas-melt equilibria. *Chem Geol* 213:265–280
- Morizet Y, Paris M, Gaillard F, Scaillet B (2010) C-O-H fluid solubility in haplobasalt under reducing conditions: an experimental study. *Chem Geol* 279:1–16
- Mysen BO, Popp RK (1980) Solubility of sulfur in $\text{CaMgSi}_2\text{O}_6$ and $\text{NaAlSi}_3\text{O}_8$ melts at high-pressure and temperature with controlled f_{O_2} and f_{S_2} . *Am J Sci* 280(1):78–92
- Newman S, Lowenstern JB (2002) VOLATILECALC: a silicate melt- $\text{H}_2\text{O-CO}_2$ solution model written in Visual Basic for excel. *Comp Geosci* 28:597–604
- Nicholis MG, Rutherford MJ (2009) Graphite oxidation in the Apollo 17 orange glass magma: implications for the generation of a lunar volcanic gas phase. *Geochim Cosmochim Acta* 73:5905–5917
- Nowak M, Behrens H (1995) The speciation of water in haplogranitic glasses and melts determined by in situ near-infrared spectroscopy. *Geochim Cosmochim Acta* 59:3445–3450
- Nowak M, Behrens H (1997) An experimental investigation of diffusion of water in haplogranitic melts. *Contrib Mineral Petrol* 126:365–376
- Oppenheimer C (2003) Volcanic degassing. In: Rudnick RL (ed) *The crust. Treatise in geochemistry*, vol 3. Elsevier, Amsterdam, pp 123–166
- Parat F, Holtz F, Feig S (2008) Pre-eruptive conditions of the Huerto Andesite (Fish Canyon System, San Juan volcanic field, Colorado): influence of volatiles (C-O-H-S) on phase equilibria and mineral composition. *J Petrol* 49:911–935

- Ripley E, Li C, Moore CH, Elswick K, Maynard JB, Paul RL, Sylvester P, Seo JH, Shimizu N (in press) Analytical methods for sulfur determination in glasses, rocks, minerals and fluid inclusions. In: Behrens H, Webster JD (eds) Sulfur in magmas and melts and its importance for natural and technical processes, vol 74. Rev Mineral Geochem
- Scailliet B, Pichavant M (2003) Experimental constraints on volatile abundances in arc magmas and their implications for degassing processes. In: Oppenheimer C, Pyle DM, Barclay J (eds) Volcanic degassing, vol 213. Geol Soc Spec Pub, pp 23–52
- Scailliet B, Pichavant M (2005) A model of sulphur solubility for hydrous mafic melts: application to the determination of magmatic fluid compositions of Italian volcanoes. *Ann Geophys* 48(4–5):671–698
- Scailliet B, Clemente B, Evans BW, Pichavant M (1998) Redox control of sulfur degassing in silicic magmas. *J Geophys Res* 103(B10):23937–23949
- Scailliet B, Luhr JF, Carroll MR (2003) Petrological and volcanological constraints on volcanic sulfur emissions to the atmosphere. *AGU Geophys Mono* 139:11–40
- Silver LA, Ihinger PD, Stolper E (1990) The influence of bulk composition on the speciation of water in silicate glasses. *Contrib Mineral Petrol* 104:142–162
- Spilliaert N, Metrich N, Allard P (2006) S-Cl-F degassing pattern of water-rich alkali basalt: Modelling and relationship with eruption styles on Mount Etna volcano. *Earth Planet Sci Lett* 248(3–4):772–786
- Tamic N, Behrens H, Holtz R (2001) The solubility of H₂O and CO₂ in rhyolitic melts in equilibrium with a mixed CO₂–H₂O fluid phase. *Chem Geol* 174:333–347
- Teague AJ, Kohn SC, Klimm K, Botcharnikov RE (2008) Sulphur solubility in Mount Hood andesites and CO₂ fluids: implications for volcanic degassing. *EOS Trans. AGU*, 89(53), (Fall Meet. Suppl. Abstract V21B-2086)
- Wallace PJ, Carmichael ISE (1994) S speciation in submarine basaltic glasses as determined by measurements of SK α X-ray wavelength shifts. *Am Miner* 79:161–167
- Wallace PJ, Edmonds M (in press) The sulfur budget in magmas: evidence from melt inclusions, submarine glasses, and volcanic gas emissions. In: Behrens H, Webster JD (eds) Sulfur in magmas and melts and its importance for natural and technical processes, vol 74. Rev Min Geochem
- Webster JD (1992a) Fluid-melt interactions involving Cl-rich granites: experimental study from 2 to 8 kbar. *Geochim Cosmochim Acta* 56:659–678
- Webster JD (1992b) Water solubility and chlorine partitioning in Cl-rich granitic systems: effects of melt composition at 2 kbar and 800°C. *Geochim Cosmochim Acta* 56:679–687
- Webster JD, Botcharnikov RE (in press) Distribution of sulfur between melt and fluid in S-O-H-C-Cl-bearing magmatic systems at shallow crustal P-T conditions. In: Behrens H, Webster JD (eds) Sulfur in magmas and melts and its importance for natural and technical processes, vol 74. Rev Min Geochem
- Webster JD, Sintoni MF, De Vivo B (2006) The role of sulfur in promoting magmatic degassing and volcanic eruption at Mt. Somma-Vesuvius. In: De Vivo B (ed) *Volcanism in the Campania plain*, vol 9. Elsevier, Amsterdam, pp 219–233
- Webster JD, Sintoni MF, De Vivo B (2009) The partitioning behavior of Cl and S in aqueous fluid- and saline-liquid saturated phonolitic and trachytic melts at 200 MPa. *Chem Geol* 263:19–36